Digital Core Analysis as an Efficient Tool for Acid Treatment Optimization

Evgeny Ivanov[1*], Dimitry Korobkov[1], Igor Varfolomeev[1], Alexander Demianov[1], Alexander Sidorenkov[1], Anna Beletskaya[2], and Mikhail Stukan[1]

[1]Schlumberger, 125171 Leningradskoe shosse 16A, build. 3, Moscow, Russian Federation

[2]Schlumberger, 555 Industrial Boulevard, Sugar Land, TX 77478, USA

Abstract. Digital rock workflow for acid treatment optimization is developed. It includes construction of a digital rock model based on X-ray microtomography, running a set of multiscale digital experiments and a number of acid flooding experiments on rock samples for the model tuning. Here, we present results of application of the developed workflow for Austin chalk rock treatment by hydrochloric acid on core samples of 8 mm in diameter. Pore-scale simulations were performed using high-resolution 3D microCT models to determine the dependencies of rock permeability, active surface area and effective reaction rate on actual porosity. These properties were used to populate the laboratory-size core models, and Darcy-scale numerical approach was applied to simulate the dissolution at different injection rates. The core-scale simulations demonstrated inhomogeneous character of dissolution process leading to wormhole development in a certain range of injection rates. In parallel to numerical simulations, laboratory experiments on the same rock samples were performed at flow rates close to the optimal regimes followed by microCT imaging of wormhole structures. This information was then used to tune the model parameters. After that, the dependencies of the number of pore volumes injected until the breakthrough (PVBT) on the injection rate were obtained numerically for all the cores considered.

1 Introduction

Acidizing is one of the approaches widely used to increase the rate of hydrocarbons production from carbonate reservoirs. The effect is achieved due to partial dissolution of matrix rock by acid solution injected under pressures below the formation fracture pressures. Depending on parameters, such as reactive fluid composition, rate of fluid injection, and rock mineral composition, different dissolution patterns can be created. Face dissolution is observed when the acid is spent before penetrating deep into the rock. While uniform dissolution takes place, when the acid is evenly distributed along the treatment zone leading to uniform increase of rock porosity. The optimal inflow of hydrocarbons toward the wellbore or fracture is achieved, when the acid creates a set of thin channels, or so-called wormholes.

The treatment efficiency is crucially dependent on the acid composition and injection scenario. Since the optimal parameters are determined by geology and lithology of the reservoir, to achieve the best effect, each treatment should be preceded by experiments on representative rock samples.

One of the key characteristics determined in the framework of acidizing job design is the pore volume to breakthrough (PVBT). Which is defined as the amount of treatment fluid (measured in core pore volumes) required to be injected before the appearance of macroscopic channel on the opposite side of the core. PVBT dependence on the treatment fluid injection rate goes through the minimum, which reflects the optimum injection rate [1, 2].

Standard design of acidizing job heavily relies not only on laboratory experiments, but also on the simulation of treatment fluid impact on transport properties of the rock. Among the parameters to be optimized are the treatment fluid composition, sequence of injected fluids, amount of the fluid to be injected, and the injection rate. These simulations base on geology model of the near wellbore zone of the collector and account for fluid-rock interactions via such effective parameters as PVBT, which have to be determined in core experiments. Unfortunately, the amount of the core material available is usually not sufficient for comprehensive laboratory analysis of various fluids and treatment scenarios. Moreover, the destructive nature of acidizing experiments imposes the fundamental limitation: experiments are performed on different core samples, which makes impossible any direct comparison of different acidizing scenarios. Conventional laboratory acidizing experiments performed using insufficient number of samples are less conclusive, since it is hard to distinguish the effects caused by the changes in the treatment scenario from those related to the variation in sample properties without averaging over a sufficiently large collection of samples. Therefore, a potential added value of simulation-based screening of acidizing scenarios for performance of acidizing technology can hardly be overestimated. Development of numerical models applicable for acidizing optimization have been of high interest during the past decades [3, 4]. According to the recent review [5], most available acidizing models do not provide acceptable accuracy in prediction of the optimum

* Corresponding author: EIvanov7@slb.com

injection rate. One of the possible reasons is that due to the limitations in computational resources, reactive transport models cannot simultaneously account for spatial heterogeneity at different scales: from macro scale, down to the pore scale. Thus, to make predictions on scales interesting from a practical point of view, the well-mixed condition is often assumed at scales smaller than the model discretization size. Similarly, many semi-empirical models assume the existence of dominant wormhole and ignore fine-scale acidizing patterns [3]. Therefore, using those models, one cannot properly reproduce the actual wormhole patterns and hence identify the optimum acid composition and fluid injection rates. We believe that a proper digital acidizing model should be able to reproduce the laboratory results scales, under a wide range of experimental conditions — only then such a model can be considered as a verified one and used at practically interesting scale.

There are definite indications that rock pore structure is a critical factor in carbonate acidizing job design [6, 7, 8]. Dubetz et al. [6] have shown that pore size distribution functions can correlate with optimal acidizing parameters better than porosity or permeability.

In acidizing processes, the transport phenomenon interferes with the chemical reaction. This determines the size and the resolution of a model required — it must capture the pore space geometry before and after the treatment and describe the whole physical sample.

Here, we propose a combined two-scale approach based on detailed digital rock models obtained using X-ray microCT. The pore scale approach used in this work is based on a combination of principles of thermodynamics and density functional theory applied for hydrodynamics (DFH) [9]. This approach allows to estimate the effective reactive and transport properties of the rock directly from the pore geometry and the treatment fluid properties [10] and is not restricted to any specific treatment fluid or mineral. The inhouse simulation software (Direct Hydrodynamics (DHD)) we use for pore-scale simulations, proved to be applicable in many problems of HC recovery from the porous media [11-13].

In our previous work [12], we described implementation of the heterogeneous chemical reactions at pore scale accounting for the evolution of pore geometry during reactive flow. However, accounting for all the fundamentals of treatment process makes the developed algorithm computationally expensive. Therefore, it was applied at small models of porous media sufficient to capture just few connected pore channels.

In the current work the pore-scale simulations were used in assumption of fixed pore geometry just to calculate the transport and reactive properties in each individual sub model, obtained from detailed microCT scan of carbonate rock. Results of numerous calculations were used to correlate the relative active surface and permeability to porosity in order to use these correlations in core-scale modeling.

The continuum model was utilized to simulate the reactive fluid flow using the Darcy equation on core scale. To capture the mineral dissolution process, the closing relations for the effective reaction rate and evolution of rock transport properties were defined from the direct hydrodynamics modeling at pore scale.

The developed approach allows to effectively account for the core-scale phenomena and the presence of fine pores in low-permeable matrix in the models, which contain high permeable structures like fractures and wormholes. It also allows to upscale the treatment fluid–mineral rock chemical reaction from pore scale to the continuous Darcy-scale modeling.

In this work, we demonstrate an application of the suggested approach on example of Austin chalk core samples treatment with aqueous solution of hydrochloric acid.

This paper is organized as follows. First, the summary of laboratory core tests is presented. Then the microCT scan equipment and digital model construction technique is described, followed by numerical model description. Finally, the results of laboratory tests together with numerical simulations are discussed and followed by conclusions.

2 Experimental setup

While analyzing heterogeneous reservoir rocks, it is important to perform laboratory measurements and microCT imaging on the same core plug. Taking into account the constrains of both techniques the Ø8 mm plug with 10-20mm length looks like an optimal tradeoff between the image quality and the suitability of the sample for the laboratory experiments. We use existing routine core analysis (RCAL) and special core analysis (SCAL) methodology and equipment adapted for the cores of such size [14].

A special configuration of 3-phase core flooding setup was assembled for the test (Fig. 1). For flooding experiments on mini-plugs, we built a Hassler-type core holder with electrodes for electrical properties measurements by two-wire method. In the mini plug flooding experiment, the pressure drop can be measured between inlet and outlet only because of small plug length.

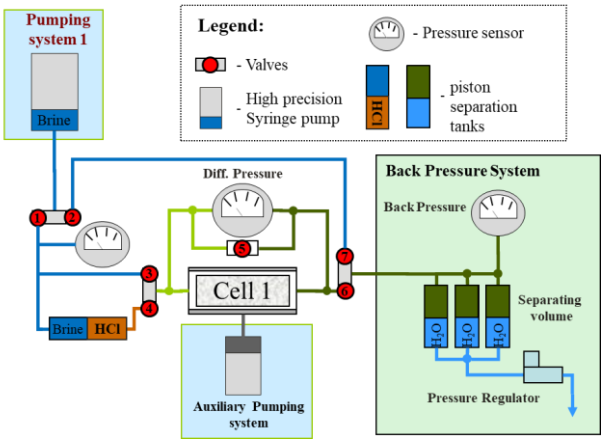

Fig. 1. Hydraulic scheme of coreflooding setup.

The outer part of the core holder is connected to auxiliary pumping system to maintain confining pressure.

Core flooding setup consists of the following main parts (see Fig. 1):

• Main pumping system with two precision syringe pumps for constant pulseless fluid injection with the flow rate range 0.001 to 30 ml/min at pressure up to 40 MPa.

• Separation tank connected through valve 4 to core inlet. Prior to the experiment, it is filled with acid. During the experiment, acid is displaced into the line and comes to the core.

• Inlet fresh line connected through valves 1 and 3 to core inlet. It is used for the initial core flooding, stabilization of the flow and for flash after acid pumping.

• Auxiliary line between valves 2 and 7. It is used to fill up back pressure system before the test.

• Back pressure system to maintain pore pressure at core outlet at constant level in range 1 to 40 MPa.

• Differential pressure measurement system (includes a couple of gauges and safety bypass with valve 5) placed between inlet and outlet of the core holder for precision pressure drop measurements (±0.0003 MPa) along the studied core.

Multiphase core flooding system was simplified for the acidizing test. It was found that a single pumping system that provides the constant flow rate directly (for brine injection) or through a separation tank (for acid) is much better than two independent pumping systems for injection of brine and acid. At the single pump configuration, one can benefit from pulseless swap of flow from brine to acid and back.

3 Acid flooding experiments on Austin Chalk core samples

For acidizing experiments, we chose well known carbonate outcrop called Austin chalk. This rock is rather homogeneous in terms of mineralogy and void space geometry at least on millimetre to centimetre scale. Gas permeability values of the studied carbonate miniplugs were in range 11.3 to 18.0 mD at porosity 23.2 to 28.6 %.

As a model brine we used 2 %wt solution of NaCl, while solution containing 15 %wt of HCl and 2 %wt of NaCl was used for acidizing.

Before acidizing test, a mini-plug was fully saturated with model brine using vacuum saturator and then loaded into the core holder. Temperature, as well as confining and pore pressures were gradually increased to the target values in a course of one hour. The described series of the experiments was done at ambient temperature (~27° C), 70 bar pore pressure (i.e. back pressure in Fig. 1) and 110 bar confining pressure. Listed pore pressure was chosen to reduce the effect of the evolved CO_2 gas while acidizing.

Experiment was started with measurement of single-phase water permeability (100 % of brine in flow) at different flow rates. After flow stabilization at the required flow rate (i.e. pressure drop along the core became constant), the inlet valves 3 and 4 (Fig. 1) were switched to allow acid flow instead of brine flow.

After injecting the required amount of acid solution, the valves were switched again to injection of brine to flash out and stop the acidizing process. Upon completion of the experiment and drying the sample, amount of dissolved/removed mineral was calculated based on the sample weight before and after the experiment.

Electrical resistivity of the core was measured by two-point method during all flooding experiments and the measured value was used to estimate the time when the acid front came to the miniplug inlet.

It is extremely important for miniplug acidizing to reduce dead volume of tubes at core inlet, i.e. between outlet of valves 3, 4 and miniplug inlet. Otherwise, mixing of the acid solution and brine leads to the decrease of the acid concentration at the front. This can significantly influence the results of the rock dissolution. In our test we minimized the dead volume to 0.3 ml to guarantee close to a step-function rapid increase of acid concentration at the core inlet.

Mutual analysis of pressure and electrical resistivity data during the experiment allowed to determine the basic parameters of carbonate acidizing process, including the beginning of the wormhole generation and its breakthrough at the opposite end of the sample. When the acid front approaches the core inlet, the electrical resistance begins to decay. In general, the acid injection is stopped as soon as the differential pressure drops to zero, indicating that the core is fully penetrated by high permeable dissolved wormhole. Depending of the flooding test purpose, the acid flow could be stopped early. Early stop of the acid injection gave us opportunity to study using microCT the wormhole structure at different stages of its evolution.

Two carbonate miniplugs (Exp2, Exp3 – target samples) were chosen for laboratory test and for digital model constructions and simulation, while one additional miniplug (Exp1 – trial sample) was prepared from a similar rock sample for preliminary measurements of PVBT and possible adjustment of experiment scenario for the target cores. Parameters of the core samples and experiment scenarios are listed in Table 1.

Table 1. Description of core samples and laboratory tests

	Exp1*	**Exp2**	**Exp3**
Core size L / Ø mm	17.7 / 7.6	16.7 / 7.7	16.4 / 7.7
Porosity	23.2 %	24.3 %	26.6 %
Permeability	9.1 mD	12.2 mD	15.8 mD
Pore volume	0.187 ml	0.186 ml	0.204 ml
Pre-test measurements		High-res. microCT	
Acid flooding test scenario	1) saturation with brine 2) flow stabilization 3) injection of 15 % HCl @ 0.4 ml/min		
	until BT reached	0.2ml injected	0.1ml injected
	4) cleanup		
Post-test measurements	Porosity measurement and microCT to determine wormholes structure		

*Trial sample

Standard PVBT measurement implies acid injection until the rapid pressure drop at inlet gauge, which

conforms to corresponding permeability increase. Unfortunately, the acid located within the core and line at that moment dissolves additional mineral during the cleanup stage, resulting in overdeveloped wormholes structure. To minimize this effect, we measured an approximate value of PVBT on the trial sample and adjusted the volumes of acid injected on the target cores.

Electrical resistivity measurement allows to detect acid front approaching the face of core sample, where electrode is placed, and thus eliminates the effect from dead zone of holder before the core. Fig. 2 demonstrates a resistivity decrement after approximately 0.33 to 0.35 ml of acid is injected.

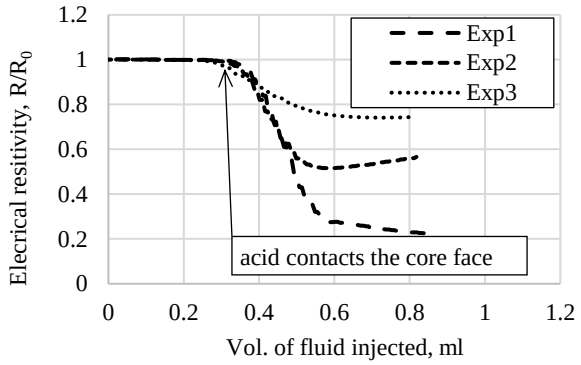

Fig. 2. Electrical resistivity of the cores during fluid injection. The start of resitivity decrease corresponds to the contact of acid front with the core face (shown by callout).

Pressure profiles during acidizing process (difference between inlet and outlet valves) are shown in Fig. 3. The moments the acid front contacted the cores faces are marked to demonstrate the difference between the amount of acid required to breakthrough the core and the total volume of acid injected to the moment. For the trial sample, BT was achieved at 0.58 ml of acid injected, but only ~0.24 ml actually came into the core at that time. Experiments on the target cores were adjusted and only 0.2 and 0.1 ml of acid were injected; sharp pressure leaps at the corresponding moments (see Fig. 3) indicate valves switching. The actual acidizing of target cores took place during the cleanup phase, when brine was injected into core holder. Brine injection lasted for about tens of pore volumes until the core properties became stable.

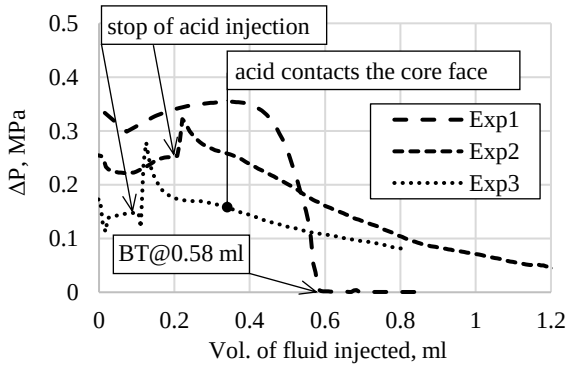

Fig. 3. Differential pressure (between inlet and outlet valves) as measured during acidizing process in all experiments. Acid injection was started at zero and stopped at specific for each core volume (shown by callouts).

The post-acidizing core parameters were measured after full cleanup on dried cores (see Table 2).

Table 2. Core measurements after acid flooding experiments

	Exp1*	**Exp2**	**Exp3**
Core size L / Ø mm	17.7 / 7.6	16.7 / 7.7	16.4 / 7.7
PVBT	2.4 ml (1.3 PV)		
Porosity (increment)	31.7 % (+8.5 %)	26 % (+1.7 %)	27.6 % (+1 %)
Permeability (relative incr.)	>10 D ×1000	1.4 D ×115	980 mD ×62

* For the trial sample the values of porosity and permeability don't correspond to the wormhole breakthrough, since the acid injection wasn't stopped at BT, full amount of acid injected was ~3.5PV

4 Core imaging and pore-scale calculations

For all samples 3D images both before and after the acid treatment were obtained using Bruker™ SkyScan™ 1172 microCT scanner with a maximum 10 W tube power and 100 kV tube voltage, at "step and shoot" sample rotation type and 0.1° rotation of sample per step. For the Ø = 7.7 mm, L = 16.4 mm miniplug, we achieved ~2.2 μm voxel size. It means that the whole sample comprises of ~4000×4000×8000 voxels in total. It should be noted that the charge-coupled device (CCD) detector installed in this microCT got 4000×2096 pixels, and the conventional circular scanning trajectory [15] was used – each sample was scanned as a sequence of overlapping vertical segments that were stitched together after the Filtered back projection (FBP) reconstruction. We compensated for gentle slow changes in X-Ray tube brightness and beam hardening artefacts using spatially smoothed histogram matching for large cylindrical regions.

The core flooding process was performed outside of the microCT; thus, the acquired images were not spatially aligned. We used in-house developed software [16] to spatially register the "before acid" and "after acid" images. Spatial registration allows direct voxel-to-voxel image comparison (Fig. 4), as well as comparison of actual and simulated wormhole geometries.

We built binary pore/void models (Fig. 5) for both "before acid" and "after acid" images using a modified image segmentation method, based on indicator kriging [17]. In this work, we assumed that the regions of the sample that were far enough from the wormhole were not affected by the acid. This allowed to automatically optimize the "after acid" image segmentation parameters by minimizing the pixelwise mismatch between both binary images within such a region. The binary models of the wormholes were built based on the difference between

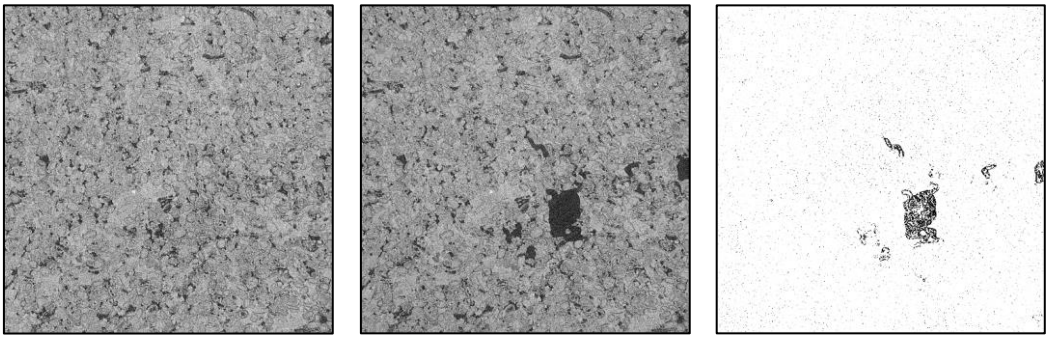

Fig. 4. Fragments of the spatially registered microCT images (from left to right): before acid treatment, after the treatment, and their absolute difference.

spatially registered models of core before and after acidizing experiment (Fig. 4).

Each full-sample model was cropped into a regular grid of 425 non-overlapping 396^3 sub-blocks, which were used to model numerically the rock properties using the in-house developed software for high-resolution digital model analysis based on the principles of DFH [9]. An example of 396^3 block with noticeable changes on its top face is shown in Fig. 5.

The permeability calculation implies obtaining the steady-state solution for velocity distribution within resolved pores with proper (no slip) boundary conditions on the faces of rock cells together with holding fixed overall flow rate through the model. Such calculation requires iterations and may be computationally expensive for big models of large core sample. But, for the needs of the current work, we calculated velocity distribution on cubic models of moderate size (see Fig. 6) to investigate statistics of properties distribution, so permeability calculations were relatively cheap in terms of computational resources and could be processed in parallel. In addition, we calculated porosity and active surface of mineral over the same sub-models, to construct proper correlations in order to utilize them for construction of the core-scale model.

Automatic parameters finetuning improves overall results consistency. Even though for some individual sub-blocks the data obtained looked counterintuitive, e.g., the open porosity decreased after the acid treatment (Fig. 7). Although this is physically possible, e.g., due to non-dissolvable particles migration, in the current study it is likely that such events should be attributed to image imperfections (e.g., noise). Provided that such effects are inevitable, fairly large statistics are required to mitigate their influence on the final result.

It should be noted that all "before acid" blocks had porosity between 7.5 to 15% (Fig. 8). That is significantly below the lab measurement results (Table 1), which can be associated with large amount of below-resolution porosity. However, the calculated permeability remained within 5 to 50 mD range (Fig. 8), which aligns with the laboratory data fairly well. Thus, we assumed that the larger-pores network, responsible for the most part of the flow rate was resolved well enough for adequate transport modeling. This allowed us to limit ourselves to simple binary models on this stage, avoiding additional higher-resolution scanning, multiscale model construction, and calibration steps [13].

An example of 396^3 block with significantly altered porous structure is shown in Fig. 5 and Fig. 6. The "before acid" permeability of this block is only 8 mD, while the "after acid" permeability is 75 mD. Meanwhile, the resolved porosity changed from 10 % to 13 %, and the open porosity changed from 6 % to 11 %. Note the high-velocity region next to the (local) tip of the wormhole — this was the major flow channel even before the acid treatment, and the local flow rate significantly increased after the treatment.

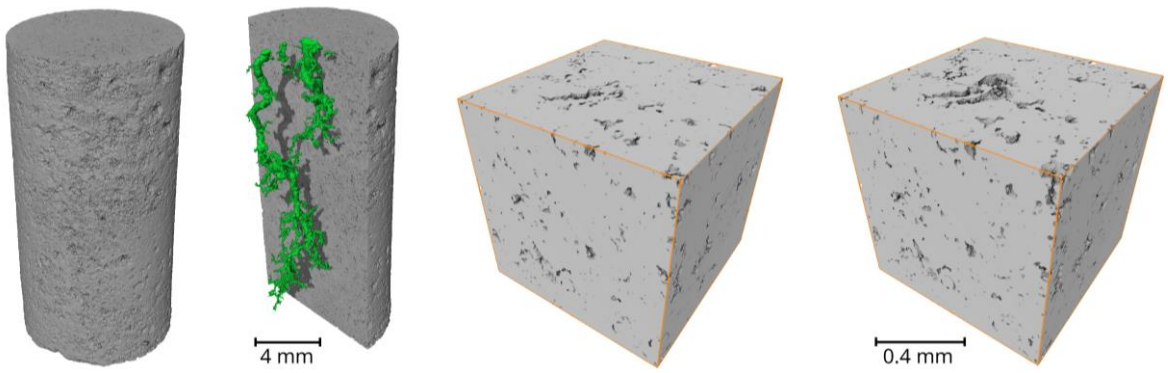

Fig. 5. 3D renders of the binarized microCT images of Exp3 sample (from left to right): full ~4000×4000×8000 voxel "before acid" state, spatially registered "after acid" state (with wormhole shown in green), example of inner 396^3 voxel cube in "before acid" state, the same cube in "after acid" state.

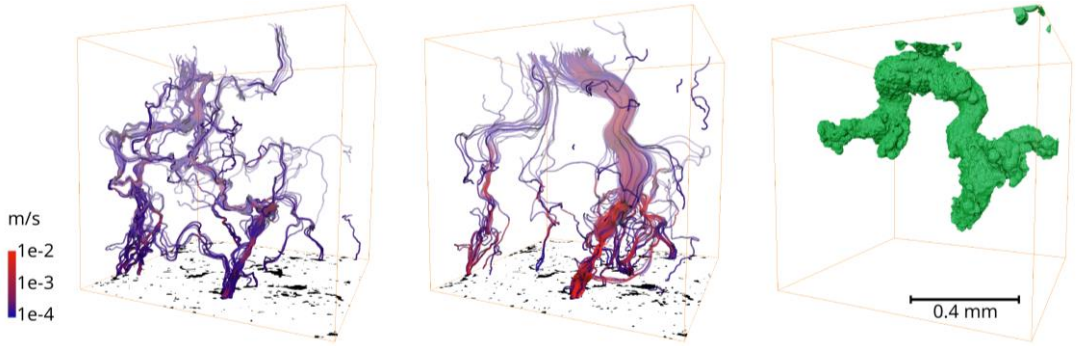

Fig. 6. Streamlines from single phase digital flow simulations on two spatially registered 396^3 voxel binary models, shown in Fig. 5: "before acid" (left) and "after acid" (middle). Semi-transparent part of the flowlines next to the top face of the cube correspond to the flow source. Fluid velocity is color-coded in logarithmic-scale units. The dissolved volume is visualized on the right.

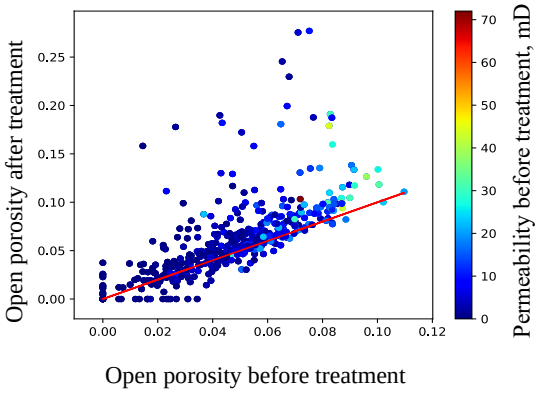

Fig. 7. Crossplot open porosity before and after the acid treatment, with color-coded permeability for individual 396^3 blocks. Note that mostly-dissolved blocks featured higher porosity and permeability even before the acid treatment. Red line is $y = x$.

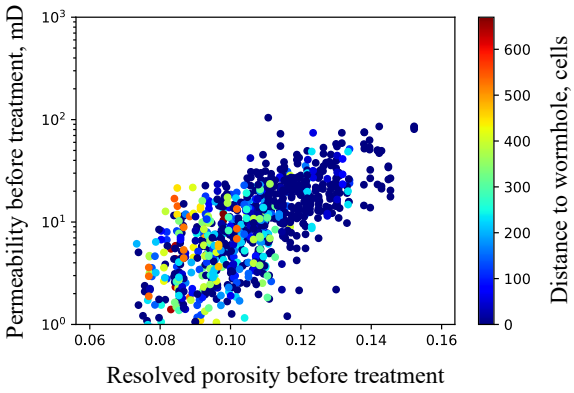

Fig. 8. Permeability vs porosity crossplot, with color-coded distance to wormhole for individual 396^3 blocks. Note that wormhole is generally passes through blocks with high porosity and high permeability.

5 Pore-scale model

Reactive flow modeling is computational resource intensive. Thus, we downscaled full sample ~4000×4000×8000 voxel binary models to just ~200×200×400 voxel models, where each voxel encoded local porosity (Fig. 9) (that is, the average of the corresponding 20×20×20 region of the original image). Instead of binary pore/mineral representation of the core, each voxel in such a model is associated with an initial permeability value in accordance with its intrinsic porosity, based on the porosity-permeability correlation plots obtained on pore-scale models.

As it was mentioned above, parameters of the pore-scale model were adjusted to represent spatial inhomogeneity of core properties and its evolution during dissolution process.

Resolved porosity (φ_{res}), as it follows from the results of numerical analysis of core models, constitute only ~1/3 of total porosity (φ_{tot}) measured. Deficient unresolved porosity (φ_{unres}) was distributed uniformly over the solid mineral; the new total porosity, given by the following equation, should match the value measured in laboratory experiment (see Table. 1):

$$\varphi = \varphi_{res} + (1 - \varphi_{res}) \cdot \varphi_{unres}$$

In actual work, we adopted the correlation proposed by Maheshwari et al. [2]. The properties of porous media were assumed to be linked to the open porosity according to the two-parametric dependence:

$$\frac{K}{K_0} = \left(\frac{\varphi}{\varphi_0}\right)^{\gamma} \left(\frac{\varphi(1-\varphi_0)}{\varphi_0(1-\varphi)}\right)^{2\beta} \quad (1)$$

$$\frac{r_p}{r_{p0}} = \sqrt{\frac{K\varphi_0}{K_0\varphi}} \quad (2)$$

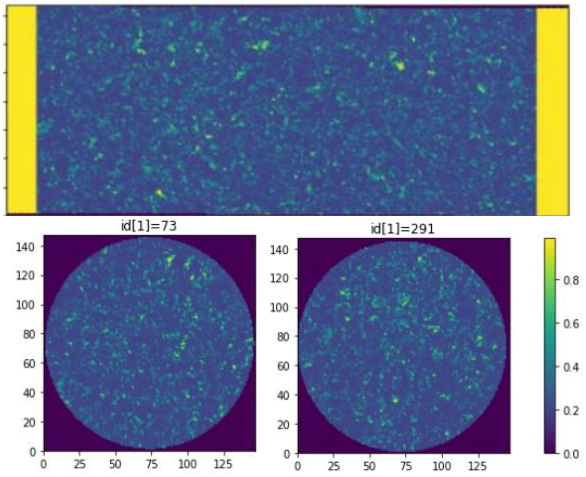

Fig. 9. Downscaled model of Ø8 mm core (Exp3) before acizing. The porosity (after correction to account for the unresolved pores) distribution is shown by color within longitudinal and cross sections, dark zones are impermeable walls of coreholder, bright yellow are spacers between inlet/outled sides of coreholder and core faces. Voxel size is 50 μm.

$$\frac{a_v}{a_{v0}} = \frac{\varphi r_{p0}}{\varphi_0 r_p} \tag{3}$$

Here, φ is porosity including unresolved one, K is absolute permeability, r_p is average pore radius, and a_v is active surface area available for heterogeneous reaction per unit volume of porous media. Variables with index 0 denote values with respect to initial (reference) state of the porous media. Exponents β and γ are pore-broadening and pore-connectivity parameters; they are estimated using the properties of the rock. It should be noted that permeability increases infinitely while mineral dissolving, while porosity converges to 1.0 as defined by eq. (1). In order to avoid infinite values in equations, the actual value of permeability should be limited at some reasonable level. In the current work we applied upper limit for permeability at level of the 75-90% of dissolved porosity.

Table 3. Parameters of the pore-scale model described by eqs. (1-3)

	Exp2	**Exp3**
$\varphi_{unresolved}$	18.3%	20.2%
φ_0^*	27%	
K_0, mD	19	
a_0, m^{-1}	$1.8 \cdot 10^4$	
β	2	
γ	1	

6 Core-scale reactive flow model

For core scale modeling we utilized continuous media approach instead of direct hydrodynamics within complex pore space geometry, used for pore scale simulations.

In the current work, reactive flow modeling is formulated in accordance with well-known continuous model of transport in porous media, assuming the local mass velocities to be defined by Darcy law. Our formulation accounts for chemical reactions, which are responsible for the porosity increase due to dissolution of mineral, and changes in the solution composition, due to spent of active component of acid. The reactions are governed by kinetic law defined by reaction rate in dependence on local concentration of acid, relative area of active surface of the mineral in contact with acid, and in general it may vary with flow rate and pore channels structure.

Before providing governing equations, let us specify basic variables used in continuum mechanics to describe instantaneous state of mixture: component molar densities n_i (index i denotes the component number ($i = \underline{M}ineral, \underline{W}ater, \underline{A}cid, reaction \underline{P}roduct$)), pressure P, spatial Cartesian coordinates $a = x$, y or z, and time coordinate t. We considered isothermal processes, so the temperature was assumed to be fixed, and dependence of certain variables on temperature was omitted. We will use the shortened notation $\partial_t B \stackrel{\text{def}}{=} \partial B/\partial t$ for partial derivatives with respect to coordinates and time, as well as the summation over repeated indexes is implied hereinafter (e.g., $\partial_a I_{ia} \stackrel{\text{def}}{=} \frac{\partial}{\partial x} I_{ix} + \frac{\partial}{\partial y} I_{iy} + \frac{\partial}{\partial z} I_{iz}$).

Upscaling from distinguished individual pores to Darcy description implies reformulation of transport properties, reaction kinetics, and mineral dissolution to continuous representation of porous media [18, 19]. In the framework of this approach, the common conservation equations are the following:

$$\partial_t(\varphi n_i) + \partial_a I_{ia} = q_i = \eta_i r_{eff}, \tag{4}$$

$$I_{ia} = n_i U_a + Q_{ia},$$

$$U_a = -\frac{K_{ab}}{\mu}\partial_b P,\ Q_{ia} = -\varphi D_{i,ab}\partial_b n_i,$$

$$\partial_t \varphi = -\eta_M v_M r_{eff}, \tag{5}$$

where $r_{eff} = r_{eff}(n_i, S_a, u)$ is the rate of the effective chemical reaction of mineral dissolution, which accounts for mixture composition, mineral-acid contact area S_a, and the flow rate u. Here, U_a is the seepage velocity component along the axis a; $D_{i,ab}$ is the effective diffusion tensor, including dispersion of velocity within porous media; η_M and v_M are stochiometric coefficient and mineral molar volume, respectively.

In the current work, we used a simplified model of fluid components (pseudo components) and reaction kinetics. First, we assumed the reaction rate to be dependent on a single component (acid) only. Therefore, calculation of the transport equation for the other components could be avoided, since the distribution of reaction products didn't affect the result. Also, the fluid was considered as incompressible; hence, any change of the fluid volume is either due to porosity increase or due to generation of new volume of fluid during reaction. This can be expressed by a source term in continuous equation:

$$\partial_t \varphi + \partial_a U_a = \eta_i v_i r_{eff}, i \in \{W, A, P\}$$

That is solved in form of general elliptic problem on pressure distribution:

$$\frac{1}{\mu}\partial_a (K_{ab}\partial_b P) = -\eta_i v_i r_{eff}, i \in \{M, W, A, P\} \quad (6)$$

The sum $V_r = \eta_i v_i$ could vary depending on the experiment conditions and, moreover, during the dissolution process (if non-ideal solution model is applied), since molar volumes of components are functions of mixture composition.

The certain form of permeability K_{ab} and dispersion $D_{i,ab}$ tensors, as well as the effective reaction rate as a function of rock properties and flow rate serve as the closing relation for eqs. (4)-(6) and should be obtained from experiments and pore-scale modeling.

7 Numerical approach to core-scale reactive flow modeling

Our implementation of the reactive flow in porous media modeling can be divided into two computationally expensive parts: pressure distribution calculation and solution of mass transfer equations with chemical reactions. The problem of pressure determination inside each voxel of the simulation domain can be reduced to the solution of a system of linear equations (6). In the current implementation, we used generalized minimal residual method (GMRES) solver with multigrid preconditioner from NVIDIA AmgX library, which gives an opportunity to utilize GPU accelerators.

We utilized an explicit algorithm for mass transfer calculations. The developed algorithm had first-order approximate precision for space and time steps and was implemented both for parallelized calculations on CPUs or GPUs. CPU realization used Numba library for python and was tested on 48 cores. GPU version utilized a single graphical card for better performance – enabling parallelization on several GPUs allowed to enlarge the grid size, but on the price of calculation speed. The CPU version showed good performance while using up to 12 cores. With larger core count, it became less effective. GPU utilization significantly improved mass transfer calculation performance: modern GPUs showed approximately 9 times speed up compared to 12 CPU cores (see Table 4 and Fig. 10).

Table 4. GPU calculation performance.

GPU	Execution time (ms per call)	GPU memory usage (GB)
Pressure calculation step		
Tesla V100	180	1.065
Tesla P100	260	1.052
Tesla K40	670	0.666
Transport+reaction calculation step		
Tesla V100	0.97	0.125
Tesla P100	1.10	0.125
Tesla K40	3.98	0.125

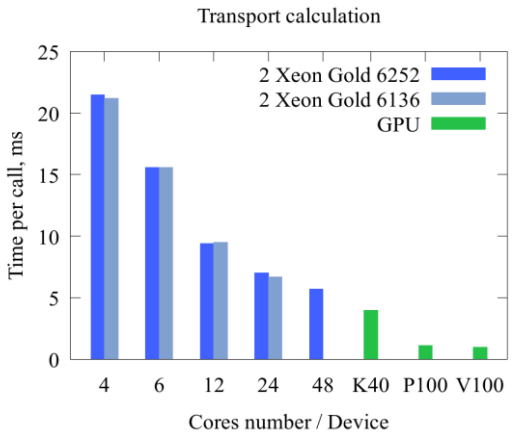

Fig. 10. Time required for transport equations calculation procedure at different CPUs and GPUs.

We performed several tests to determine performance of our code on different hardware. For tests, we used model with 184×75×75 grid cells. Since pressure calculation is the most computationally expensive part of the algorithm (see Table 4), it was performed once per certain number of simulation steps according to the changes in permeability due to chemical reactions. In the test case, 10000 transport steps were made, and it required 54 pressure updates. This proportion (54:10000) heavily depends on the simulated domain structure and can vary starting from 1:10000 to 1:10 reflecting the wormhole propagation.

According to the tests performed, a GPU version is preferable for better calculation speed, however, the grid size is limited by GPU's memory capacity. For modern P100 and V100 accelerators, it is about 13.8M (~440*176*176) voxels in a simulation domain. Preferable solution to overcome this limitation is optimization of algorithm for pressure solver to minimize possible performance lost on parallelized GPUs.

8. Acidizing modeling and results analysis

Core-scale digital models of each of the sample cores (see Table 1) were constructed and tuned as described in the previous sections. Results of laboratory tests were used to adjust such parameters as effective reaction rate and diffusion, which are hard to be measured experimentally. Although it is possible to estimate the dependence of the effective reaction rate on active surface area (and indirectly, porosity), acid concentration and fluid injection rate from the digital models, the exact value of the effective reaction rate cannot be defined without additional experiments. Similarly, the construction of acid diffusion/dispersion model, which accounts for heterogeneity of fluid velocity and mixing of fresh acid and reaction product with brine, also requires labor-intensive experiments. Though such highly elaborated approach, which requires a series of laboratory and numerical experiments for parameters tuning is known [20], in the current work, we decided to utilize simplified reaction/diffusion models, taking into account only the mobility of the components and effective

interaction between them at given experimental condition, without considering their chemical nature. This enabled building a practically applicable model that reproduced the experimental result without numerous laboratory experiments; however, its application is limited to certain combination of acid, mineral and experiment conditions. Therefore, the respective models should be adjusted for each study.

Equations for reaction and diffusion applied in the current work are as follows:

$$r_{eff} = k_{eff} S_a n_A \quad (7)$$

$$D_{i,ab} = D_{acid}\, I_{ab} \quad (8)$$

Where k_{eff} is the heterogeneous reaction rate coefficient, S_a is the active surface area per unit volume of porous media, while n_A is calculated as concentration of acid per unit volume of fluid, D_{acid} is the diffusion coefficient of the effective component of the acid solution, and I_{ab} is the identity matrix.

The simulation parameters (see Table 5) were determined based on the experiment conditions or tuned iteratively for the best match between the simulation results and respective experimental data for treated cores.

Table 5. List of simulation parameters.

Parameter	Unit	Value
brine/acid solution viscosity, μ	mPa*s	0.84
acid component diffusion, D_{acid}	m^2/s	$1.5 \cdot 10^{-9}$
stochiometric coefficients		
mineral η_M		-1
acid η_A		2
water η_W		-4
reaction products η_P		1
molar volume	m^3/mole	
mineral v_M		0.06357
acid v_A		0.03064
water v_W		0.018
reaction products v_P		0.1501
heterogeneous reaction rate, k_{eff}	m/s	$4 \cdot 10^{-3}$

In the simulations the moment wormhole break through the core outlet was determined geometrically, unlike to the experimental approach, where PVBT was measured by pressure difference. The connected region(s) of core, where porosity is increased up to the limit (determined in the separate sensitivity study) of 95-99%, was defined as wormhole(s), and the length of such region(s) from the inlet face to its farthest tip was the parameter indicating the wormholed part of the core.

Simulation of the acidizing process on each of digital core models was performed in accordance with experimental workflow. Trial sample was acidized at fixed acid flow rate (0.4 ml/min) and PVBT value was measured and compared with the experimental value. Variations of the reaction rate and acid component diffusion coefficients allow to amend the wormholes structure and resulting PVBT value in a wide range. However, in the current study the values close to the reported in literature [19,21] worked rather well.

After the acidizing model parameters were determined at the cores-scale digital model of the first trial core, experiments on target cores were performed with limitation of injected acid volume in agreement with the laboratory workflow.

As the result for each core model, the PVBT value, final porosity distributions, total amount of dissolved rock, permeability, and wormhole geometry were obtained and compared with the experimental data.

Table 6 summarizes the result of experiments and respective simulations in terms of PVBTs and core after-treatment porosities and permeabilities. The observed systematic deviations between experimental and simulated permeability may be caused by neglecting transition from Darcy to Navier-Stokes flow in big caverns and dissolved wormholes. The correct accounting for viscous effects in open channels would require solution of vector non-linear Navier-Stokes equation in such regions which would result in overconsumption of memory and computational time. The necessary optimizations and improvements are the subject of further research.

Table 6. Simulation results and respective experimental data

	Exp1	Exp2	Exp3
Volume of acid injected	PVBT measure	0.2 ml 1.1 PV	0.1 ml 0.5 PV
Laboratory measurements on treated core			
PVBT	1.3PV		
Porosity		26%	27.6%
Permeability		1.4 D	980 mD
Simulation			
Porosity		25.6%	27.5%
Permeability		1.1 D	760 mD
PVBT at 0.4ml/min		1.1PV	1.34PV

The final wormhole structures obtained for two target cores in simulations and in experiments (build based on microCT interpretation) are shown in Figs. 12 and 13.

Pairwise comparison of wormholes images corresponding to simulations and experiments shows qualitatively similar patterns, however plenty of disturbances in details are also clear. In general, it may be explained by insufficient quality (resolution and noise) of models obtained from microCT and applied for numerical simulation and due to the fact that in numerical simulations we did not account for Navier-Stokes flow in channels. However, it is possible to assume that the major heterogeneous features of rock were properly captured in the digital models, since the trends are reproduced fairly well, and integral characteristics after the acid treatment are close to the ones measured on physical core samples.

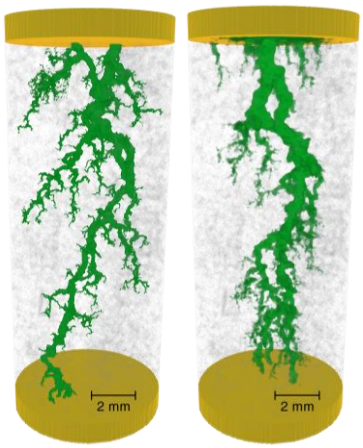

Fig. 12. Wormhole patterns obtained after Exp2 laboratory acidizing experiment (left) and the corresponding digital simulation (right). Yellow zones represent inlet/outlet space.

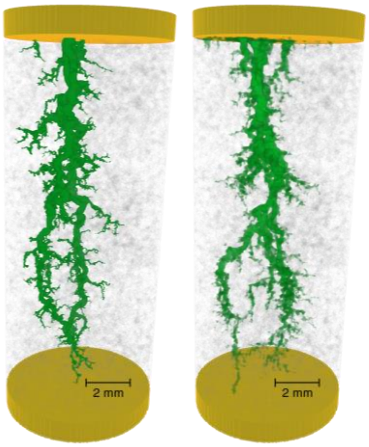

Fig. 13. Wormhole patterns obtained after Exp3 laboratory acidizing experiment (left) and the corresponding digital simulation (right). Yellow zones represent inlet/outlet space.

The simulated streamlines (Fig. 14) within core/wormhole show the flow distribution during the acidizing experiment. As the wormhole propagation approached the end, the maximum velocity speed increased for several orders of magnitude. Because of that, the calculation performance also drastically decreased closer to the end of simulation, due to limitation on the time step of explicit scheme.

Digital experiment allows to repeat simulations at varying fluid injection rates in a wide range from 0.04ml/min to 1ml/min. As the result, the PVBT curves for two cases were obtained (see Fig. 15).

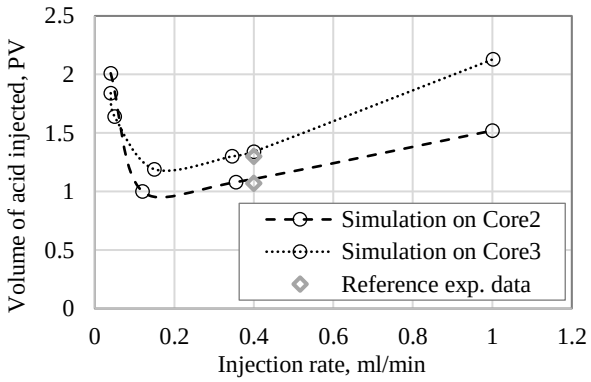

Fig. 15. PVBT curves obtained on digital cores together with reference laboratory data.

Conclusions

In this study, we analyzed carbonate acidization process using the two-scale continuum model. We simulated reactive flow of acid in carbonate rock at Darcy scale, while the accounting for the underlying physics at the pore level was performed through direct pore-scale simulation of transport properties on micromodels of real rocks. To tune rock models and demonstrate predictive capability of the present approach, the PVBT and dissolution patterns were obtained from numerical simulations and compared with experiments on Ø8mm cores of Austin Chalk. Also, PVBT curves in a wide range of injection rates were calculated on the same core models, which would be impossible in the laboratory due to the destructive nature of the experiments. The suggested approach opens the way for improvements in acidizing job design by increasing the consistency between the models used the for reactive flow modeling and actual pore-scale structure of the real rocks.

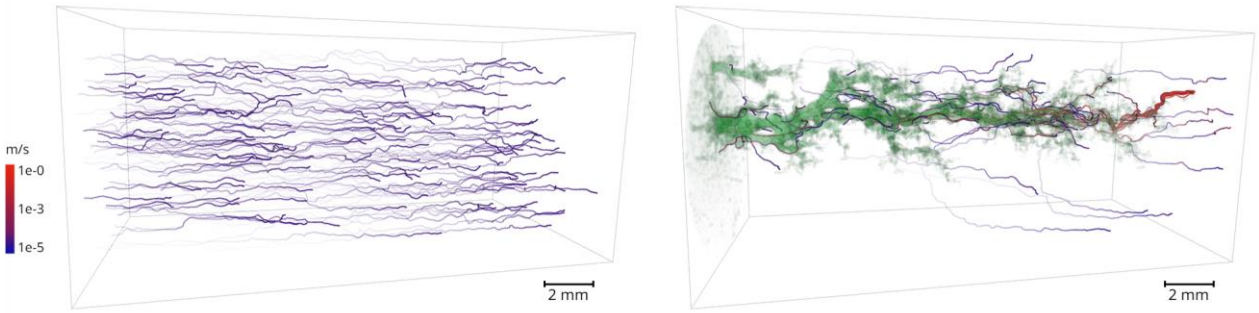

Fig. 14. Simulated streamlines from single-phase core-scale flow modelling (Exp3) with color-coded velocity and semi-transparent simulated wormhole (in green), before the acid treatment (left) and after (right).

References

1 C.N. Fredd, H.S. Fogler, *SPE Formation Damage Control Symposium*, SPE-31074-MS (1996)

2 P. Maheshwari, R.R. Ratnakar, N. Kalia, V. Balakotaiah, Chem. Eng. Science 90 258–274 (2013)

3 G. Glasbergen, N. Kalia, M.S. Talbot, *8th European Formation Damage Conference, Scheveningen*, SPE-121464-MS (2009)

4 C.I. Steefel, et al, Computat Geosci. 19 (3): 445–478 (2015)

5 O.O. Akanni, H.A. Nasr-El-Din, *SPE Middle East Oil & Gas Show and Conference*, SPE-172575-MS (2015)

6 D. Dubetz, et al, SPE Annual Technical Conference and Exhibition, SPE-181725-MS (2016)

7 J. Etten, D. Zhu, A.D. Hill, *EUROPEC* SPE-174314-MS (2015)

8 M.E. Ziauddin, E. Bize, SPE Middle East Oil and Gas Show and Conference, SPE-104627-MS (2007)

9 A. Demianov, O. Dinariev, N. Evseev, Introduction to The Density Functional Method in Hydrodynamics (Moscow: Fizmatlit, 2014)

10 E. Ivanov, et al., *SPE Russian Petroleum Technology Conference*, SPE-202016-MS (2020)

11 A. Demianov, O. Dinariev, N. Evseev, Can. J. Chem. Eng. 89 (2): 206–226, (2011)

12 A. Beletskaya, et al., *SPE Russian Petroleum Technology Conference*, SPE-187805-RU (2017)

13 O. Dinariev, N. Evseev, D. Klemin., *E3S Web Conf*. 146 01001 (2020)

14 D. Korobkov, A. Goncharov, *Society of Core Analysts*, SCA2014-081, (2014)

15 Andrew M. Kingston, et al., Proceedings Volume 9967, Developments in X-Ray Tomography X; 996712 (2016)

16 A. Nadeev, "Method For Evaluating Material Sample Structural Changes Resulting From Acting Upon Sample", WO2016013955

17 W. Oh, B. Lindquist, IEEE Transactions on Pattern Analysis and Machine Intelligence, Volume: 21, Issue: 7, (1999)

18 M.K.R. Panga, M. Ziauddin, V. Balakotaiah, AIChE Journal 51 3231–3248 (2005)

19 M. Ghommem, et al., Journal of Petroleum Science and Engineering 131: 18-33 (2015)

20 M. Ghommem, W. Zhao, S. Dyer, Journal of Modeling and Simulation Vol.5: 63-71 (2014)

21 M. Gautelier, E.H. Oelkers, J. Schott, Chemical Geology 157 (1-2): 13–26 (1999)